batteries

Article

Impact Testing of Aging Li-Ion Batteries from Light Electric Vehicles (LEVs)

Miguel Antonio Cardoso-Palomares [1], Juan Carlos Paredes-Rojas [2], Juan Alejandro Flores-Campos [3], Armando Oropeza-Osornio [4] and Christopher René Torres-SanMiguel [1,*]

[1] Instituto Politécnico Nacional, Escuela Superior de Ingeniería Mecánica y Eléctrica, Sección de Estudios de Posgrado e Investigación, Unidad Zacatenco, Mexico City 07738, Mexico
[2] Instituto Politécnico Nacional, Escuela Superior de Ingeniería Mecánica y Eléctrica, Unidad Culhuacán, Mexico City 04440, Mexico
[3] Instituto Politécnico Nacional, Unidad Profesional Interdisciplinaria en Ingeniería y Tecnologías Avanzadas, Mexico City 07340, Mexico
[4] Instituto Politécnico Nacional, Escuela Superior de Ingeniería Mecánica y Eléctrica, Unidad Ticomán, Mexico City 07340, Mexico
* Correspondence: ctorress@ipn.mx

Abstract

The increasing adoption of Light Electric Vehicles (LEVs) in urban areas, driven by the micromobility wave, raises significant safety concerns, particularly regarding battery fire incidents. This research investigates the electromechanical performance of aged 18650 lithium-ion batteries (LIBs) from LEVs under mechanical impact conditions. For this study, a battery module from a used e-scooter was disassembled, and its constituent cells were reconfigured into compact modules for testing. To characterize their initial condition, the cells underwent cycling tests to evaluate their state of health (SOH). Although a slight majority of the cells retained an SOH greater than 80%, a notable increase in their internal resistance (IR) was also observed, indicating degradation due to aging. The mechanical impact tests were conducted in adherence to the UL 2271:2018 standard, employing a semi-sinusoidal acceleration pulse. During these tests, linear kinematics were analyzed using videogrammetry, while key electrical and thermal parameters were monitored. Additionally, strain gauges were installed on the central cells to measure stress and deformation. The results from the mechanical shock tests revealed characteristic acceleration and velocity patterns. These findings clarify the electromechanical behavior of aged LIBs under impact, providing critical data to enhance the safety and reliability of these vehicles.

Keywords: electromobility; abuse tests; mechanical impact; LEVs; micromobility; LIBs

check for updates

Academic Editors: Pascal Venet, Haifeng Dai, Dongdong Zhao, Grzegorz Sierpiński and Bo Jiang

Received: 12 May 2025
Revised: 7 July 2025
Accepted: 8 July 2025
Published: 13 July 2025

Citation: Cardoso-Palomares, M.A.; Paredes-Rojas, J.C.; Flores-Campos, J.A.; Oropeza-Osornio, A.; Torres-SanMiguel, C.R. Impact Testing of Aging Li-Ion Batteries from Light Electric Vehicles (LEVs). *Batteries* **2025**, *11*, 263. https://doi.org/10.3390/batteries11070263

Copyright: © 2025 by the authors. Licensee MDPI, Basel, Switzerland. This article is an open access article distributed under the terms and conditions of the Creative Commons Attribution (CC BY) license (https://creativecommons.org/licenses/by/4.0/).

1. Introduction

Currently, unsustainable urban development accounts for 70% of global Greenhouse Gas (GHG) emissions, with urbanized areas contributing 23% [1]. The trend is that by 2030, it will increase by 20%, and by 2050, it will increase by 50% [2]. According to the United Nations (UN), GHG emissions cause an increase of approximately 2 °C in global temperature [3]. It also affects air quality in cities, where poor air quality poses a critical risk to the population's health, leading to pathologies in the respiratory, cardiovascular, and central nervous systems [2,4–6]. For this reason, electromobility has been proposed as an early solution to the emissions caused by transport using internal combustion engines (ICEs) [7].

One trend within electromobility that has led to an increase in the sales of Light Electric Vehicles (LEVs) is micromobility. This can be defined as the use of light vehicles powered by non-polluting energies for short trips in built-up areas [8,9]. Dependence on cars is one of the main problems in large cities worldwide, so micromobility offers a sustainable, viable, and flexible transportation alternative [10–12], in addition to improving the psychological and physical well-being of users [13]. As a result, multiple cities have promoted and implemented infrastructure for this type of transportation, leading to a significant shift in the way people get around [10,11]. Over the last 20 years, shared mobility systems have grown from fewer than 10 cities around the year 2000 to just over 2900 cities worldwide in 2021 [14,15]. Among the vehicles that can be considered within this category are powered and unpowered vehicles, such as bicycles, skateboards, and tricycles. However, there is no standard classification in micromobility vehicles; the International Transport Forum (IFT) proposes four categories to classify micromobility from a safety perspective [8]:

- **Type A:** Powered or unpowered vehicles weighing less than 35 kg and with a maximum powered design speed of 25 km/h.
- **Type B:** Powered or unpowered vehicles weighing between 35 kg and 350 kg and with a maximum powered design speed of 25 km/h.
- **Type C:** Powered vehicles weighing less than 35 kg and with a design speed between 25 km/h and 45 km/h.
- **Type D:** Powered vehicles weighing between 35 kg and 350 kg and with a design speed between 25 km/h and 45 km/h.

Likewise, in LEV classification, the European Union offers a categorization within its L-category vehicle classification system. The L1e-L3e classes cover two-wheeled vehicles, which include e-scooters, e-bikes, and e-motorcycles [9]. Since 2017, through direct sales or shared mobility platforms, LEVs have been introduced into road traffic of more than 100 cities [16]. In the United States (US), shared micromobility systems have recorded over 133 million trips in 2023, a tenfold increase in just a decade. To achieve a substantial impact on sustainability, micromobility has the following fundamental objectives: reducing GHG emissions by reducing the use of polluting vehicles, reducing costs to bridge the social gap through sustainable business models, and improving safety and infrastructure to enhance the travel experience [17]. However, this trend has brought serious security problems to the population. Quick adoption has outpaced the necessary evolution of infrastructure, traffic regulations, and public awareness, creating a new and often poorly understood safety paradigm [9]. In China, between 2013 and 2017, there were 10,000 incidents related to fires in LEV batteries, resulting in more than 200 deaths. In England, 70 fires related to this problem were reported in London in 2021, with no fatalities. In the US, between 2021 and 2022 there were 19 deaths from incidents of this type, with New York City having the most such incidents, registering 104 fires in 2021, reaching almost double the number of incidents for the following year with 6 deaths, and 13 deceases had been reported by mid-2023, with almost the same number of fires as at the end of 2022, so an upward trend is set for the following years [18]. Spielbauer et al. [19] predict that battery fire incidents and their severity will increase in the future due to two factors: the increasing energy density of new cells being developed and the growing demand for batteries to meet the EV market. Gehandler et al. [20] report that, on average, one Battery Electric Vehicle (BEV) fire occurs per year during battery charging in multi-story car parks or large garages. Meigs [18] investigates multiple fires caused by LEV batteries, from storage warehouses to apartment buildings, which have raised concerns among both the population and government authorities.

Pan et al. [21] recommend avoiding discharging the battery altogether and avoiding leaving it unused for extended periods, as this can cause premature aging and increase the risk of fatal failure.

The energy storage system of electric vehicles is responsible for supplying the stored electrical energy to the vehicle's propulsion system and secondary systems [22]. Lithium-ion batteries (LIBs) are widely used in the electromobility sector as energy storage due to their high energy density, which is significantly better than that of other types of batteries, such as lead–acid, nickel–cadmium, and nickel–metal, which were once used but have been displaced by LIBs. The energy storage system in electric vehicles can be divided into three categories: (1) The cell—the name given to an individual battery. Internally, it is composed of positive and negative electrodes, separators, and an electrolyte, embedded in a metal housing (typically steel or aluminum), with positive and negative terminals on the exterior. (2) The module—the connection of multiple cells in series or parallel, placed on polymer bases and connected with nickel-plated steel sheets welded to the cell terminals. Additionally, a battery management system (BMS) is connected and embedded in a heat-shrinkable plastic and a general housing (aluminum, ABS, or fiberglass), as required by the application. (3) The package—at this level, this is formed by combining modules, which are connected in series or parallel, depending on the application. Like the module, a battery management system is required. However, this system incorporates sensors and microcontrollers, as well as support systems (such as cooling and/or heating) to ensure its correct operation. Likewise, the package is protected by a structure with protection plates to maintain the battery's integrity in the event of mechanical impact [23,24]. According to Wang et al. and Goodman et al. [25,26], BEVs that suffer a traffic accident, can deform and/or fracture main elements of their energy storage system, which would cause failures such as disconnection between key elements, and external or internal short circuit in the cells, which could result in battery fire. The correct positioning of the energy storage system, together with an appropriate structural design, is a key parameter for electric vehicle safety [27].

In safety micromobility, the literature focuses on the injuries caused by collisions or road traffic accidents. The authors report on the severity and the body region affected by driver-users, where the upper and lower extremities are the most affected, mostly in LEVs like e-scooters, e-bikes, and conventional bikes [8]. Data from the US Consumer Product Safety Commission (CPSC) paints a stark picture, with Emergency Department (ED) visits related to e-scooters showing consistent year-over-year growth, nearly doubling in 2019 compared to the previous year. Additionally, overall micromobility injuries have increased by an estimated average of 23% annually since 2017. This trend has continued, with injuries soaring by nearly 21% in 2022 alone, accompanied by a rising number of fatalities [28,29]. In terms of collision type, there are collisions involved that occur due to loss of vehicle control or collisions with stationary objects, as well as crashes with objects in motion, such as motor vehicles, which can result in rear-end crashes or hit-and-run incidents. Another crash type involves pedestrians tripping over e-scooters or fallen bicycles [9]. However, the literature does not mention how road traffic accidents occur and what happened with the LEVs.

The safety of the energy storage systems of electric vehicles is critical for their safe use on the streets, as even the highest level of protection is insufficient to prevent fires at high speeds. Zhu et al. [30] noted that battery packs are susceptible to penetration due to sideswipe collisions and road debris impacts. In mechanical abuse, LIBs could have malfunctions, such as the breakage of the module's external and internal support elements. This can lead to the disconnection between main elements, such as the BMS with the cells, as well as the rupture of the connector plates between the internal cells, which

would cause a reduction in the voltage and energy capacity of the module. In more serious failures, an external or internal short circuit may occur in the cells due to the intrusion of conductive materials into the module. In this condition, LIBs exhibit a voltage drop and an increase in temperature, which varies depending on the type of short circuit. In external short circuits, the increase in temperature and voltage drop is progressive, which causes electrolyte leakage due to the increase in internal pressure in the cell. However, if it were to occur between the longitudinal faces of the cells, the steel would melt due to the extreme increase in temperature, which would cause a fracture in the casing, allowing the electrolyte to leak.

On the other hand, in internal short circuits, the thermal reaction is extremely violent; when an external conductive element penetrates the cell, or the internal roll is billed by the formation of dendrites due to aging, this causes conjunction between the anode and the cathode, quickly causing a voltage drop, and an increase in internal temperature and pressure, which leads to thermal runaway from the cell. At the module level, this can lead to a domino effect in the surrounding cells, as the external increase in temperature in a cell also leads to different levels of failures due to the evaporation of the internal electrolyte, from the decrease in energy capacity, to an internal short circuit due to the total evaporation of the electrolyte and the melting of the separator, resulting in thermal runaway from multiple cells. Even if the pressure inside the module or package is very high, deflagration can occur [27–32]. Zhao et al. and Larsson [33,34] found that an internal short circuit can occur for multiple reasons, such as mechanical deformations or manufacturing failures. They also observed that another reason may be the formation of dendrites within the cells that fracture the internal materials of the roll due to aging.

In fire propagation, full-scale experiments conducted in residential structures show that an e-scooter fire can cause a room to reach flashover, a state where all combustible surfaces ignite simultaneously within 30 s of the first visible smoke being emitted from the battery. The time from that first puff of smoke to a violent gas explosion can be as little as 10–20 s, making the room of origin immediately fatal and rendering escape nearly impossible [35]. For suppression fires, Torelli et al. [36] quantify the consequences of a single-cell thermal runaway failure within an e-mobility battery pack and determine the effectiveness of various suppression strategies that could be employed by a user in a home environment. Direct water cooling only partially mitigated the event by lowering the temperature and slowing the propagation, but it could not extinguish it. Fire blankets were counterproductive, failing to contain hazards while increasing pack temperature by insulating the event. The study concludes that incorporating design features, such as thermal insulation between cells, is a more robust solution for preventing thermal propagation and minimizing the severity of battery failure.

Aging in LIBs has been rigorously studied, as it undergoes a series of gradual and irreversible degradation processes. Aging leads to a reduction in nominal capacity and an increase in internal resistance (IR), which is the opposition to current flow inside the LIB. The elevated internal resistance in an aged cell is a critical factor that fundamentally alters its response to abuse. The state of health (SOH) of the battery is a quantitative parameter that measures the current state of a cell with respect to its original state. At the micro level, the presence of microcracks in the anode and cathode material, due to the formation of dendrites, can lead to serious failures such as an internal short circuit. In a 1000-cycle aging study, Goodman et al. [26] found that small-format pouch cells damaged by three-point bending often remained electrically functional despite the formation of internal short circuits (ISCs), but exhibited accelerated degradation, as confirmed by electrical characterization, Computed Tomography (CT), and post-mortem analysis. According to Santhanagopalan et al. [37], this type of failure can be presented by cells that comply

with the safety regulations implemented in industry, due to imperceptible failures in manufacturing, so it should be of special attention in future research.

A significant gap exists in the scientific literature regarding the long-term impact of mechanical stress on the safety and aging of lithium-ion batteries, a topic that has received far less attention than aging under standard operating conditions. To understand the influence of cycling on mechanical damage, Fuchs et al. [38] characterized and compared two pouch cells, one cycled and one not, after inducing deformation with a 4 mm diameter steel ball, employing post-mortem and SEM analysis for the investigation. Significantly accelerated aging was observed by Li et al. [39] in 21,700 cylindrical cells subjected to radial compressions of 3 mm and 6 mm, followed by 100 cycles. Through characterization using Incremental Capacity Analysis (ICA), Electrochemical Impedance Spectroscopy (EIS), and CT, this degradation was attributed to potential micro-leakage at the positive terminal gasket. In an experiment by Sahraei et al. [40], cylindrical 18650 LFP cells underwent rod indentation with a 6 mm diameter and 4.6 mm depth, followed by subsequent cycling for up to 89 times. After this, their performance showed no significant degradation relative to control cells.

Given the operation of Light Electric Vehicles (LEVs) in urban areas, these vehicles are not exempt from traffic accidents. Therefore, with the growing demand for this type of electric vehicle in recent years, the number of accidents due to falls and collisions with mobile or stationary objects is also expected to increase. In the context of electric micromobility, such situations are typically addressed from the perspective of injuries to the user and/or other affected individuals. However, energy storage systems based on electrochemical lithium-ion cells, such as those found in bicycles, scooters, and tricycles, can malfunction under conditions of mechanical abuse, as might occur in a traffic collision. The UL 2271:2018 standard categorizes the outcomes of such abuse into several levels of severity [41]:

- Loss of protective control.
- Electric shock hazard.
- Venting.
- Electrolyte leakage.
- Rupture.
- Fuel concentration.
- Fire.
- Explosion.

Consequently, the quantification of abuse during such an event is of significant interest, as it can trigger a battery malfunction that may lead to catastrophic failure and a hazardous situation for users and third parties.

This research aims to evaluate the electrical and mechanical parameters of 18650 lithium-ion cells within aged battery modules sourced from electric micromobility Light Electric Vehicles (LEVs). Through charge–discharge cycling tests, the SOH and IR of the cells under evaluation are determined. Subsequently, using an impact platform, a mechanical shock scenario is recreated in accordance with the UL2271:2018 standard [41] to simulate impacts the vehicle may receive, which could affect battery performance. To quantify the mechanical damage resulting from this phenomenon, the use of strain gauges affixed to the housing of the module's internal cells is proposed. Concurrently, the module's electrical parameters are monitored with a lithium-ion battery testing system to detect transient spikes. Such events could precipitate an internal short circuit and/or a rise in cell temperature, potentially triggering a cascading failure in adjacent cells that could lead to a fire or an explosion in the electric vehicle's battery module.

The article is organized as follows: Section 2 describes the experiment's design, materials, instrumentation used in the tests, and the methodology for the mechanical shock test steps. Also, the selected LEV and its battery module are presented as objects of study. Likewise, the description of the steps for manufacturing the test modules and the impact platform contemplated for the mechanical shock tests is provided. Section 3 presents the results obtained from the performance tests conducted in the cells, as well as the stresses and deformations induced by mechanical shock in the central cells of the battery modules. Additionally, the impact velocity and total acceleration received by the battery modules are presented through videogrammetric analysis. Section 4 discusses the results shown in Section 3. Section 5 presents the conclusions of the research.

2. Materials and Methods

2.1. Study Object: e-Scooter

As mentioned above, sales of LEVs have increased significantly due to the micromobility trend over the last 5 years. The best-selling LEVs globally are e-bikes, e-scooters, and mopeds. For this reason, a pre-owned e-scooter (Citycoco Harley) that has been in use since 2019 was selected. Multiple Chinese automakers have manufactured this e-scooter model, so the assembly origins are unknown. The LEV is presented in Figure 1, and its specifications are in Table 1.



Figure 1. Study object (**a**) Citycoco Harley e-scooter; (**b**) 60 V–12 Ah battery module; (**c**) Li-ion cell LXD18650 20P3.

Table 1. Technical specifications: Citycoco Harley 2019 e-scooter.

Parameter	Value
Motorization	BLDC Hub motor—1000 W
Energy storage system	Two Li-ion battery modules 60 V–12 Ah
Mass	80 kg
Maximum velocity	40 km/h
Autonomy	60 km
Load capacity	200 kg
Brake system	Front and rear hydraulic disk brakes
Dimensions	1.85 × 0.8 × 1 m

Battery Module

As mentioned in Table 1, the LEV's energy storage system consists of two lithium-ion battery modules, each with a 60 V and 12 Ah capacity, manufactured by Hao Yang New Energy. The technical specifications of the module are presented in Table 2.

Table 2. Technical specifications: Hao Yang new energy® battery module 60 V–12 Ah.

Parameter	Value
Nominal voltage	60 V
Coulomb capacity	12 Ah
Energy capacity	720 Wh
Charge voltage	67.2 V
Maximum charging current	5 A
Maximum discharging current	30 A
Dimensions	200 × 165 × 70 mm
Production date	20 December 2018

As exterior protection and anchorage within the LEV, the battery module is housed in a polymer case. Within this module, eighty 18650 lithium-ion cells are arranged in a 16-series–5-parallel (16S5P) configuration, with a battery management system (BMS) that provides protection against overcharge and overdischarge of the internal cells. For the electrical connections between the cells, the spot-welding method was employed, utilizing 0.2 mm plates of nickel-plated steel as the conductive medium. Also, the use of polymer bases for the vertical positioning of the cells gives support and rigidity to the module. On the other hand, it is worth highlighting the use of electrical and thermal insulators, such as insulating rings positioned at the positive pole of the cells, thermal and antistatic tape for the connections between the BMS and the cells, and the use of acrylic plates as internal protection of the module. Figure 1 illustrates the disassembly process of the battery module.

The cells used inside the battery module are LXD 18650-20P3, manufactured by Zinzong LoreStar Technology Co., Ltd., Sichuan, China. In Table 3, the technical specifications of the cell can be seen. In Figures 2–4, a detailed log of charging, rate discharge, and cycling characteristics, respectively, is reported by the manufacturer on the datasheet.

Table 3. Technical Specifications: LXD 18650-20P3 battery cell.

Parameter	Value
Nominal voltage	3.6 V
Coulomb capacity	2 Ah
Energy capacity	7.2 Wh
Charge voltage	4.2 ± 0.05 V
Discharge voltage	2.75 V
Nominal charging current	0.25C (0.5 A)
Maximum charging current	1C (2 A)
Nominal discharging current	0.5 A
Maximum discharging current	6 A
Mass	43 ± 1 g
Internal resistance	≤30 mΩ
Nominal charging temperature	0–45 °C
Nominal discharging temperature	−10–60 °C

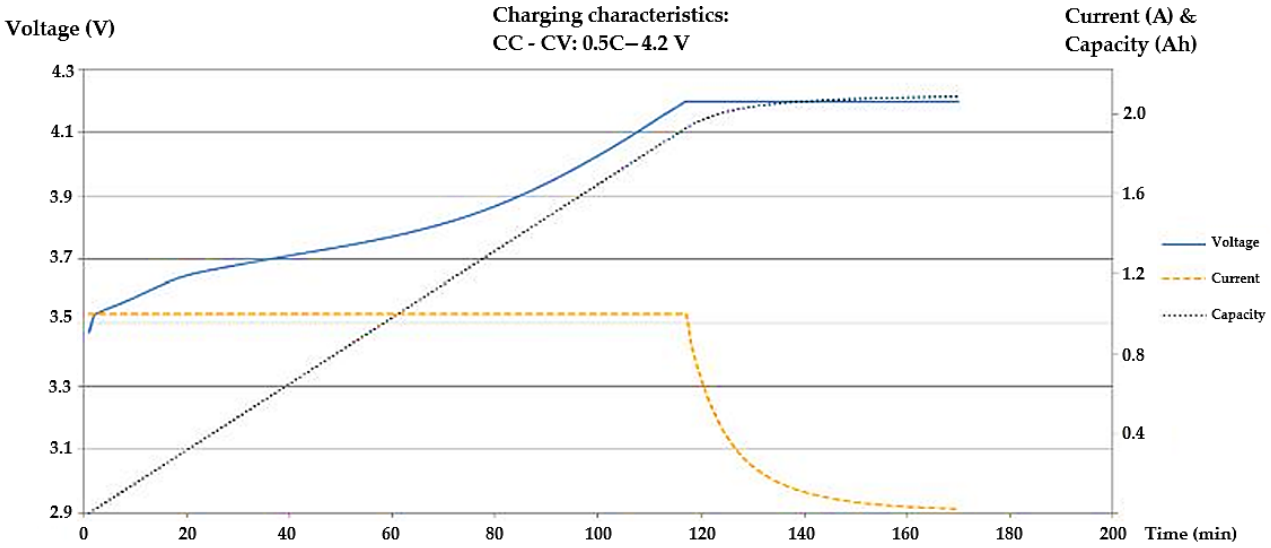


Figure 2. Charging characteristics in LXD18650 Li-ion cell.

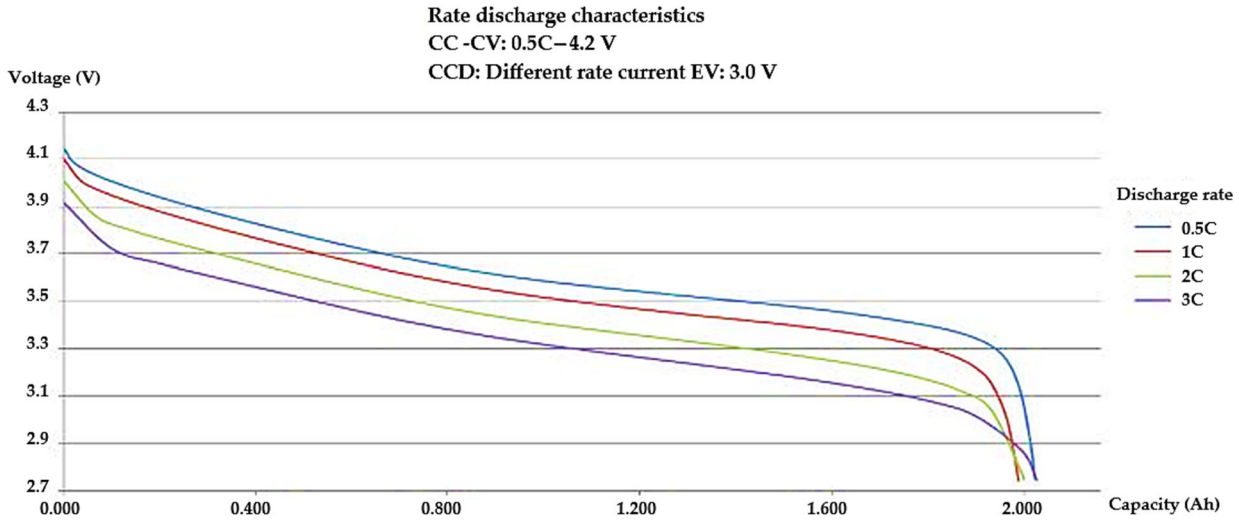


Figure 3. Rate discharge test in LXD18650 Li-ion cell.

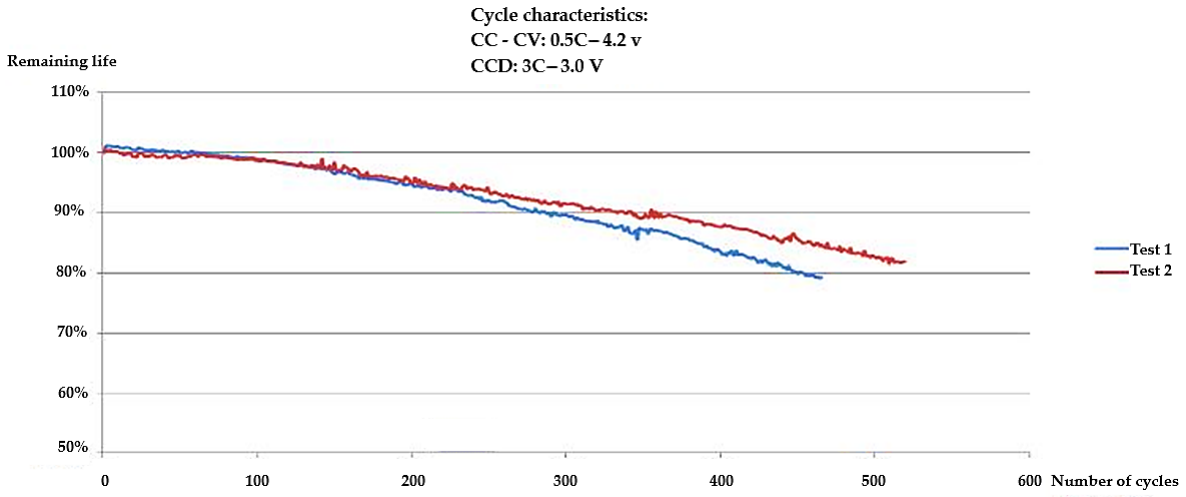


Figure 4. Cycling test in LXD18650 Li-ion cell.

In this cell, the used charging method is the constant current–constant voltage (CC/CV) method. The manufacturer reports that experiments and measurements were carried out under a standard temperature (23 ± 2 °C) and standard humidity (65 ± 20%). In Figure 2, a detailed log of charging characteristics is shown, where 1000 mA (0.5C) of CC is applied until the limit voltage of 4.2 ± 0.05 V is reached. Then, a CV phase begins, and the current starts to decrease until it reaches 20 mA (0.01C), at which point it cuts off.

In the performance test, the manufacturer tested the cell under various discharge rates (1000 mA to 6000 mA) and a cut-off voltage of 2.75 V. Charging at 1000 mA–4.2 V CC-CV is described below. Figure 3 shows the cell's voltage versus discharge capacity.

To test the cell's lifetime, the manufacturer performed cycling tests. Using the charging rate mentioned (1000 mA), and a discharging constant current rate of 6000 mA (3C) to a cut-off voltage of 2.75 V, waiting 10 min between charging and discharging, under the standard temperature and humidity conditions mentioned below. After three consecutive cycles, if the cell is ≤80% of its initial capacity, it is considered the end of its useful life. Figure 4 illustrates the percentage of lifetime versus the number of charge–discharge cycles.

2.2. Experiment Design

For this test, it is proposed to recreate a mechanical impact scenario for the battery module of an LEV. In this type of test, multiple regulations include this test within their mechanical abuse tests. The UL 2271:2018 standard focuses on the testing of LEVs, such as e-bikes and e-scooters, which fall within the classification of electric micromobility devices [8]. This standard describes initial conditions and parameters for the testing of LIBs using mechanical impact test scenarios.

- The sample battery or device under test (DUT) shall be 100% SOC and secured on all sides to the testing machine.
- The DUT will be subjected to mechanical shock in each of the six spatial directions, or, depending on the module's positioning within the LEV, to a frontal shock.
- For modules with a mass ≤ 12 kg, the test parameters are as follows:
- Pulse shape—semi-sinusoidal.
- Acceleration—50 g.
- Pulse duration—11 ms.
- During the test, the central module's temperature should be monitored.
- If the sample is still operational after the test, it must be subjected to at least one charge and discharge cycle at the maximum values recommended by the manufacturer.
- A 1 h observation period should precede this test.

Considering the above, the design of the experiment for mechanical shock tests on battery modules used in an e-scooter was developed.

As an object of study, it is proposed to use the battery module of an e-scooter, which is one of the best-selling LEV platforms worldwide [8]. To ascertain the SOH of the internal cells, the battery module was disassembled to perform cycling test on each cell. Also, it was planned to divide the internal cells into compact modules of 9 cells to perform a greater number of tests with the least number of cells involved. A constant current and voltage charging method was used to charge the modules, as indicated by the manufacturer's charging method. Moreover, the battery modules were positioned within an impact platform, taking into account their placement within the vehicle. This platform has a movable indenter at the center, with 1 DOF in the Z axis. This base has a rubber bed to achieve a semi-sinusoidal pulse, as well as elastic cords in tension that help increase the acceleration impact.

During the testing process, a slow-motion video was shot using a high-speed camera to perform a videogrammetric analysis of the linear kinematics of the mechanical shock

process on the battery module. Additionally, the use of strain gauges enables the measurement of deformations within the internal cells. Additionally, the module's temperature, voltage, and current are monitored by an electronic battery tester. Figure 5 shows an outline of the design of the experiment.

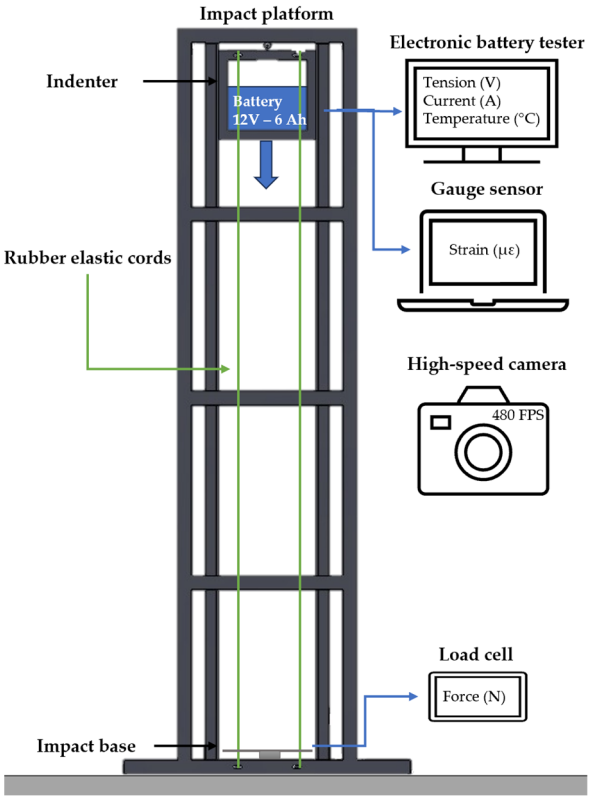


Figure 5. Experiment design.

For this purpose, a flow diagram for the experimental test is drawn up in Figure 6. In this, 5 steps are taken into consideration, which are described below. Table 4 presents the instruments used during the impact test.

Table 4. Measuring instruments used.

Quantity	Manufacturer	Instrument	Function
1	Atorch®, Guangdong, China	DL24MP-FX	Electronic battery tester: Voltage, current and temperature monitor, and capacity tester for module battery
1	Nice-power®, Shenzhen, China	SPS-E305	Adjustable power supply: Constant current and constant voltage battery charger
1	MicroMeasurements®, Wendell, NC, USA	D4 DAQ and C4A-06-G1350A-120-39P Strain gauge	Gauge strain data acquisition system: Longitudinal and circumferential micro-strain cell
1	Day Sensor®, Shenzhen, China	DY-920A DAQ and DYLF-102 Load cell	Load cell data acquisition system
1	UNI-T®, Guangdong, China	UTi-120M	Smartphone thermal camera: External battery temperature monitor
1	One Plus®, Shenzhen, China	10 pro (Sony Sensor IMX789)	High-speed recording: 720p–480 FPS

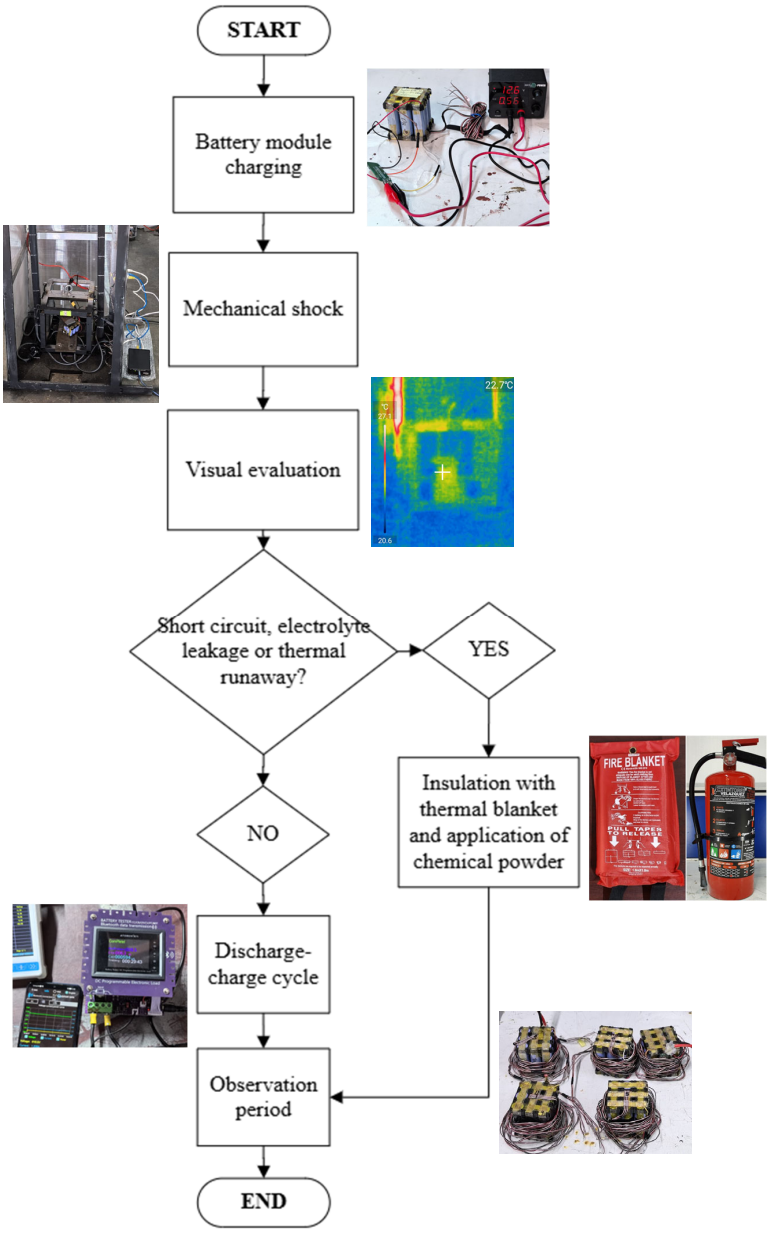
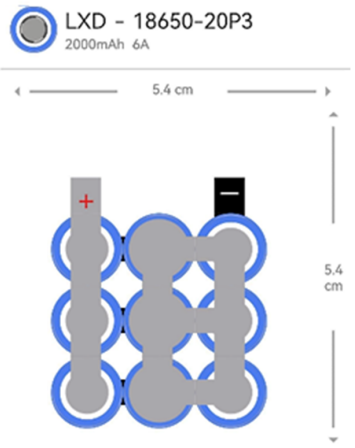


Figure 6. Methodology for impact testing.

1. **Battery module charge:** DUTs are charged to 100% SOC with an adjustable power supply according to the manufacturer's charging method.
2. **Mechanical shock:** The DUT is mounted inside the indenter, and its positioning is defined by the original module's position within the LEV, which is perpendicular to the impact plate along the Z-axis (see Table 5). After impact, the electronic battery tester monitors the DUT's electrical parameters. Additionally, the gauge strain and load cell's DAQs, as well as the video recording, begin to record the data. After that, the platform's safety bolt is released, and the DUT impact occurs.
3. **Visual evaluation:** A visual inspection of the DUT is carried out after the test to detect external short circuits, electrolyte leakage, or thermal runaway that may trigger a fire. If there is an ignition, a thermal blanket is used for isolation, and chemical powder is applied using an ABC fire extinguisher to reduce the temperature in the internal cells.

Table 5. DUT concept design.

Parameter	Value	Conceptual Design
Configuration	3s3p	
Cells quantity	9	
Coulomb capacity	6 Ah	
Energy capacity	64.8 Wh	
Nominal voltage	10.8 V	
SOC 0–100%	8.25–12.6 V	
Nominal charging current	1.5 A	
Maximum charging current	6 A	
Nominal discharging current	1.5 A	
Maximum discharging current	18 A	
Mass	0.387 kg	

4. **Discharge–charge cycle:** If the DUT does not exhibit visible damage, a discharge–charge cycle will be conducted at the rate specified by the manufacturer, with visual inspections of the module maintained throughout. Additionally, external temperature monitoring will be performed using a thermal camera at a safe distance.
5. **Observation period:** A period of observation of the module is maintained for at least 1 h. After this, it will be kept in a safe deposit box.

2.3. Work Area

For the development of this research, a work area of 12 m^2 was used inside an academic laboratory, as can see it in Figure 7. For security reasons, the work area was separated and well-ventilated to perform the cycling and impact test on LIBs. The temperature in the room and relative humidity were about 20 ± 5 °C and 50 ± 20%, respectively.



Figure 7. The work area used in the shock test.

2.4. Device Under Test (DUT)

For the DUTs, compact battery modules were manufactured with the internal cells of the electric scooter module battery. This was carried out to perform multiple tests with a single battery module and to achieve the repeatability of the results.

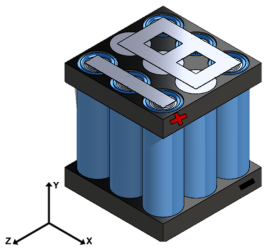
2.4.1. DUT Concept Design

As the first step in manufacturing battery modules, the conceptual design of the modules was developed. For this test, it is proposed to assemble modules of 9 cells in a 3s3p configuration, as this number of cells allows for the replication of the pattern found in modules with a central cell surrounded by eight cells on its periphery. Subsequently, the technical specifications of the cells used are required to calculate the energy capacity, charging and discharging voltages, and maximum and nominal discharge currents, as described in Table 5.

2.4.2. Detailed DUT Design

For this step, a CAD design of the battery module was created, along with a list of the main components required for module manufacture, which is presented in Table 6.

Table 6. DUT detailed design.

Quantity	Component	Detailed Design
9	LXD 18650-20P3 cell	
18	Polymeric support base	
6	Niquel connector sheet 60 mm	
6	Niquel connector sheet 40 mm	
4	Connector cable 24 AWG 50 mm	
1	BMS 3s	

2.4.3. DUT Manufacturing

Special materials and tools were used in the manufacturing of DUT. Figure 8 shows the methodology used for the DUTs assembly. The methodology steps are described below.

1. **Strain gauge installation:** For this, the installation of triaxial gauges on the cell housing was proposed to measure the deformations in the longitudinal and circumferential axes of the cell. The material used for these tests is the triaxial gauges or MicroMeasurements® rosettes C4A-06-G1350A-120-39P, which are described in Table 7, in conjunction with the D4 data acquisition system. The strain gauge used is a stacked rosette type. Figure 9 shows the 0° (A-gauge), 45° (B-gauge), and 90° (C-gauge) configuration of the strain gauge. The gauge was installed using the manufacturer's recommended bonding material and method, ensuring the correct orientation of the gauge with respect to its positive and negative terminals. **3s3p cell positioning:** A 3s3p configuration is proposed for cell positioning. In this configuration, the cell with gauge rosette installed is in the central position and surrounded by eight cells, in the same pattern found in the LEV's battery modules.
2. **Cell welding points:** For cylindrical LIBs, the spot-welding method is used to make electrical connections between the cells. This method is ideal because it does not generate excessive heat on the poles, which can cause premature wear in the cell. To achieve this, a 4 kW SUNKCO 737G spot-welding machine and a nickel-plated steel plate as the connector (10 mm × 0.2 mm) were used.

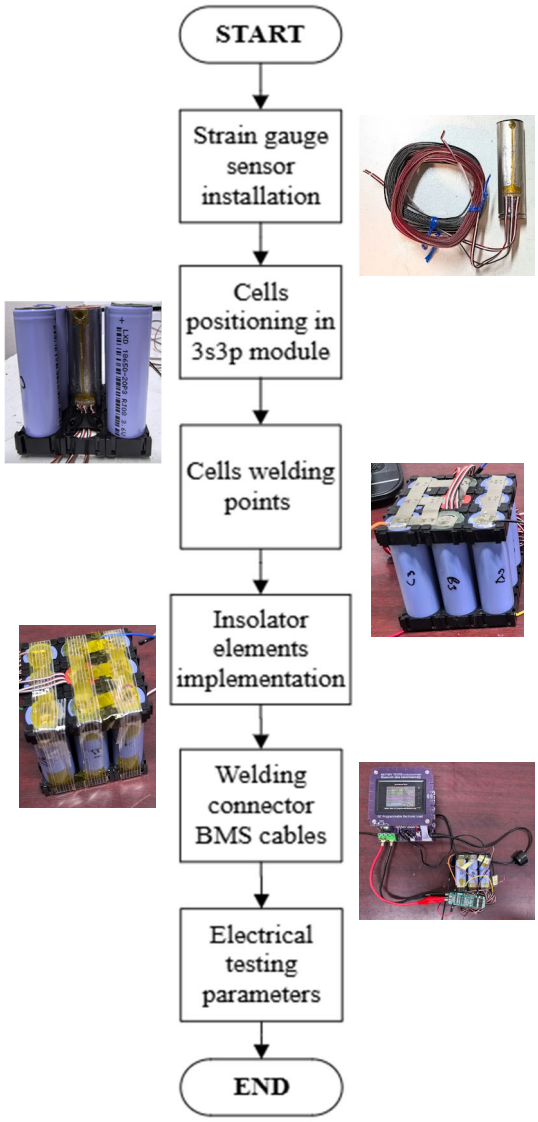


Figure 8. Methodology for DUTs Assembly.

Table 7. Technical specifications: C4A-06-G1350A-120-39P.

Parameter	Value
Resistance	120 ± 0.9% Ω
Gauge factor	1.92
Temperature range	−50–80 °C
Sensitive rosette size	5.1 × 5.1 mm

3. **Isolator elements:** The use of thermal and electrical insulation is essential, such as the use of self-adhesive joints as insulating protection in the positive terminal of the cell, BGA tape for the thermal insulation of the connections, and the use of fiberglass tape to support the cells in case of a rupture of the support bases.
4. **BMS connection:** A 3s-BMS was implemented to ensure safe management during the DUT's charge–discharge cycle.
5. **Electrical testing parameters:** To validate the correct function of the DUTs, a charge–discharge cycle is performed on each DUT. For the charging process, a constant current

(CC)–constant voltage (CV) method was used at 12.6 V–1.5 A to charge to 100% SOC. For the discharging process, a 1.5 A CC rate was applied.

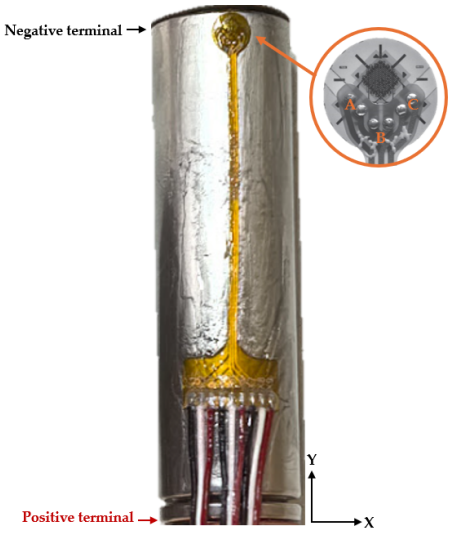


Figure 9. Strain gauge rosette orientation.

2.5. Impact Platform

The impact platform envisioned for the impact tests was manufactured in-house, as shown in Figure 10. The objective of this was to perform mechanical impact at both the cell level and the module level, which is limited to an impact area of 0.09 m^2 (0.3 m long × 0.3 m wide).



Figure 10. Impact platform used.

This platform has a simple inverted catapult design, where the indenter is mounted on two rails in a vertical position and accelerated by four elastic cords. Table 8 describes the main components of this platform.

Table 8. Main components of the impact platform.

Component	Description
Protection structure	Prismatic structure made of 1/2 × 1 1/2-inch aluminum slabs, covered on the outside by a 6 mm thick transparent polycarbonate plate as an insulating system for thermal and electrical protection.
Indenter	Square steel structure 270 mm long and 248 mm high. Made with 1 × 1/2-inch PTR profile by means of welded joints, and connected to 2 U-100 rails by means of 4 compatible forklifts with an effective travel of 2 m and powered by four rubber bungee cords. At the bottom, it has a 5 mm thick steel plate for impact against the impact base. Inside, there is a plate for holding the battery module.
Impact base	Donut-type load cell with a 5 mm thickness and a 100 mm square steel plate.

In the impact base, a Day Sensor load cell was installed to measure the impact force resulting from mechanical shock. Technical specifications and calibration details are provided in Table 9.

Table 9. Technical specifications: DYLF-102 Day Sensor® load cell.

Parameter	Value
Capacity	300 kg–2942 N
Operation temperature	−20–160 °C
Excitation voltage	5–15 VDC
Sensitivity	2.0 mV/V
Output impedance	700 Ω
Input impedance	780 Ω
Insulation resistance	2000 MΩ
Accuracy	0.05%
Nonlinearity	0.03%
Repeatability	0.03%
Hysteresis	0.03%
Test instrument	Fluke® 8041

To achieve the desired speed in the indenter, the base was anchored to the lower part of the structure by elastic rubber ropes, which allow its potential energy to be transmitted in tension to the base, which transforms it into linear movement. Those elastic cords have an elastic stiffness constant K = 313.92 N/m, which was calculated experimentally by applying a known mass of 2 kg and multiplying by the gravitational constant (a = 9.81 m/s^2), the force supported by the spring (F) is calculated; and by subtracting the initial length from the final length, the total elongation of the spring (x) is calculated; so, by means of Hooke's law, this constant can be calculated if the ropes are considered as ideal springs.

$$K = F/\Delta x \quad (1)$$

By taking the average values of the 4 strings, the elastic stiffness constant was calculated. The results are shown in Table 10.

Table 10. Calculation of the elastic stiffness constant in the ropes.

Initial Length	Final Length	Δx	K
1.0412 m	1.1037 m	0.0625 m	313.92 N/m

Likewise, the force and energy stored in tension were calculated. Equation (1) is used for the calculation of force, and the equation of mechanical work is used with Equation (2).

$$U = ½ \times K \times (\Delta x)^2 \quad (2)$$

The mass of the indenter (m), being at a certain height (h), also transfers force and energy upon impact with an object, so Newton's second law and potential energy can be used to calculate these values. Table 11 presents the total force and energy resulting from the indenter.

$$F = m \times a \quad (3)$$

$$E_p = m \times a \times h \quad (4)$$

Table 11. Force and energy calculated.

Total Force	Total Energy
1039.67 N	1649.78 J

3. Results

3.1. SOH of Internal Cells

To obtain the SOH of the module's internal cells, a charge–discharge cycle test was performed using a smart-charged XTAR®, VA, USA VC8 Gen2, as shown in Figure 11. At the first step, the initial voltage and internal resistance of the cells were measured to compare with the manufacturer's data. Subsequently, the cells were tested using the method specified by the manufacturer, as described in Table 12.



Figure 11. Cycling test in LXD18650-20P3 cells.

Table 12. Charge–discharge characteristics in the SOH test.

Parameter	Value
Charging method	CV–CC
Charging voltage	4.2 V
Charging current	1000 mA
Cut-off current	20 mA
Discharge current	1000 mA–CC
Cut-off voltage	2.75 V
Number of cycles	3
Room temperature	25 °C
Relative humidity	50%

Three cycles were performed on each cell to measure their actual capacity and calculate the average capacity. After that, the SOH of the cells was calculated using Equation (5).

$$SOH = (Q_{max}/C_n) \times 100 \quad (5)$$

where

- Q_{max} = real cell capacity (mAh)
- C_n = Nominal Cell Capacity (mAh)

In this case, the rated capacity of each cell, as reported by the manufacturer for its as-new condition, is 2000 mAh.

Figure 12 shows the plots of the electrical parameters measured and calculated for each series of internal cells. In Table A1, it can be seen that these parameters are listed by individual cell. In the following graphs, the parallel cells connected are represented from lighter to dark green (1p to 5p in each series)

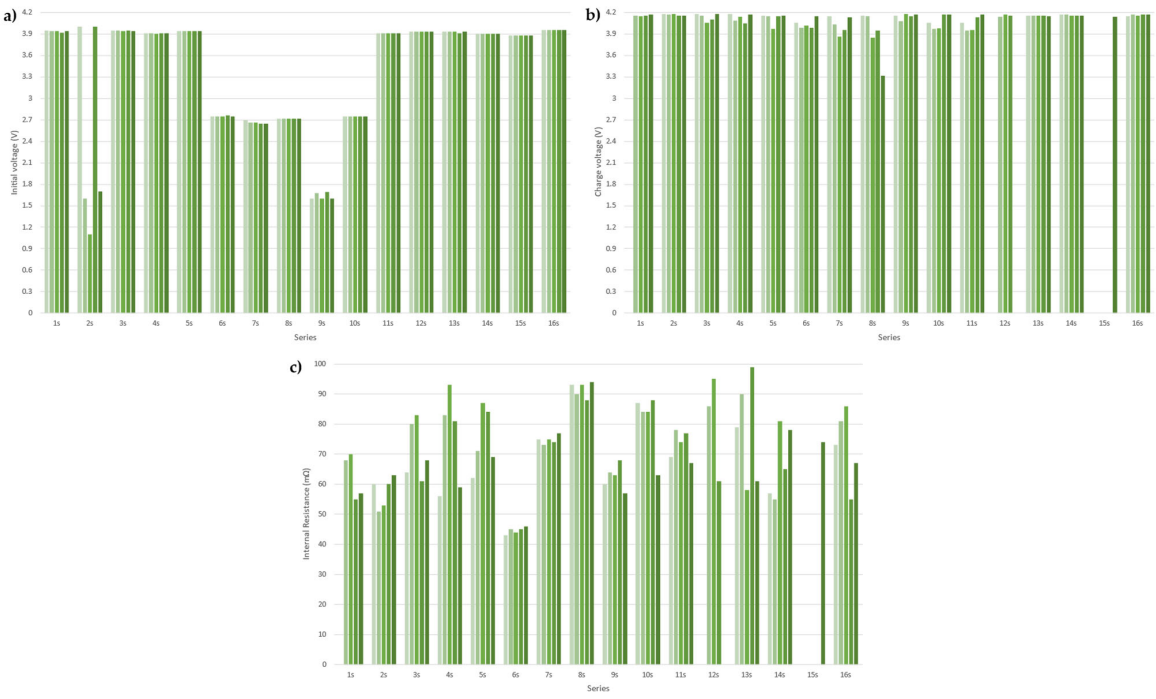


Figure 12. *Cont.*

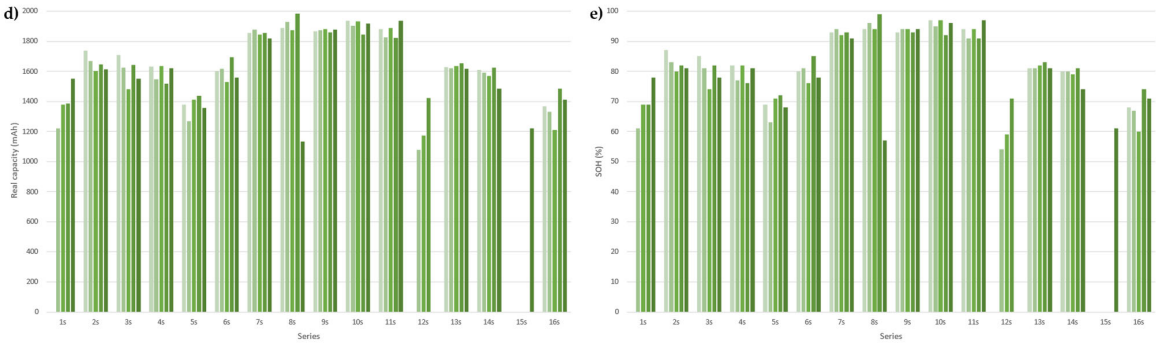


Figure 12. (**a**) Initial voltage; (**b**) charge voltage; (**c**) IR; (**d**) real capacity; and (**e**) SOH in LXD18650-20P3 cells.

3.2. Mechanical Shock Tests

For the mechanical shock test, an initial condition was proposed, as shown in Table 13.

Table 13. Initial conditions of mechanical shock test.

Parameter	Value
DUT's SOC	100%
DUT's current discharge	1500 mA CC
Indenter height	1.70 m
Cord elongation	1.93 m
Room temperature	25 °C
Relative humidity	50%

Kinematic Results

The measurement of the kinematic parameters of the indenter using videogrammetry was proposed to corroborate the platform's operation in compliance with the design parameters set by regulations and to validate the correct operation of the impact platform throughout the experimental tests. For this purpose, recordings of the platform in operation were made, and later, they were analyzed using Kinovea®, a free-to-use video study software designed for movement analysis, with a primary focus on sports science and biomechanical analysis [42]. However, due to the interface's design, it can perform movement analysis of any object, so its use in this application is convenient.

For this type of study, the quality, lighting, and fluidity of the recording are essential since the computer program with which it is analyzed collects the data in frames per second (FPS) and reference points placed on the object to be analyzed; so, by correctly controlling these three aspects, the reliability of the results obtained improve significantly. Considering the above, recording equipment and lighting suitable for recording the tests were installed to perform the experimental tests.

The results obtained from the linear kinematic analysis using Kinovea® 2023.1.2 version, are presented in Tables 14 and 15, which show the impact of velocity and pulse acceleration on each test, respectively. Figures 13 and 14 also present a comparative graph of velocity and pulse acceleration versus time.

Table 14. Impact velocity achieved in tests.

Test	1	2	3	4	5	Average	Variance	Confidence Intervals (95%)
Impact velocity (m/s)	6.89	6.59	6.76	6.74	6.89	6.77	0.015	6.619–6.929

Table 15. Pulse acceleration achieved in tests.

Test	1	2	3	4	5	Average	Variance	Confidence Intervals (95%)
G-force	23.53	21.79	22.49	22.15	23.06	22.61	0.49	21.738–23.470
Pulse duration (ms)	53	54	54	53	54	53.6	0.3	52.92–54.28

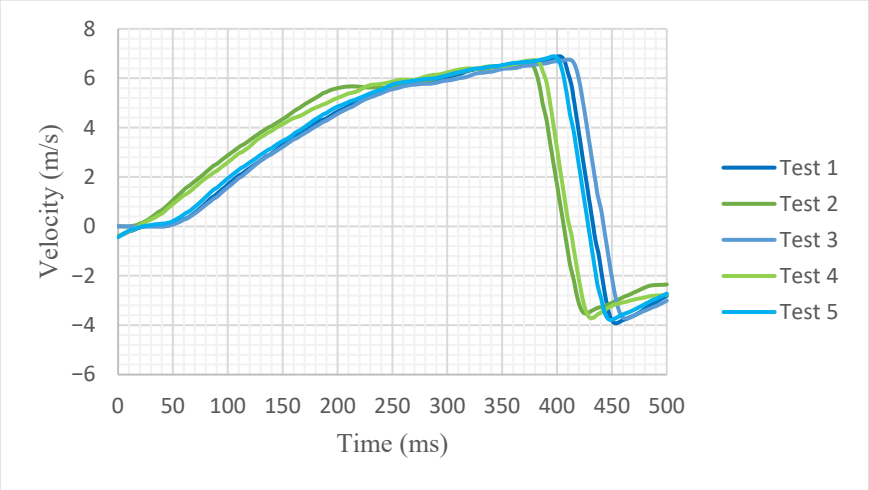


Figure 13. Comparative graph: velocity vs. time.

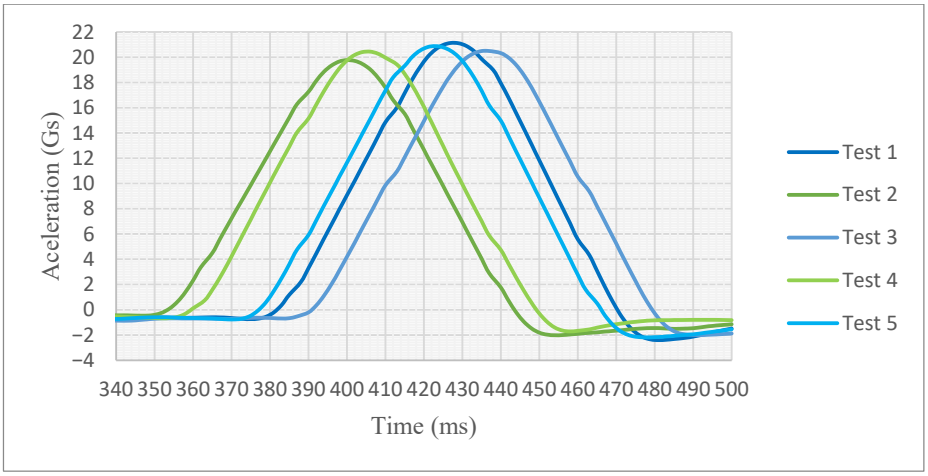


Figure 14. Comparative graph: pulse acceleration vs. time.

To register the maximum force achieved in the tests, a load cell was installed on the platform base as mentioned in Table 9 of Section 2.5 Table 16 shows the impact force resulting from each test.

Table 16. Impact force achieved in tests.

Test	1	2	3	4	5	Average	Variance	Confidence Intervals (95%)
Impact force (N)	1285	1268	1251	1399	1398	1320.2	5253.7	1230.2–1410.2

3.3. Thermal and Electrical Results

The electrical parameters and internal temperature of each module are measured during tests. As mentioned, an electronic battery tester is used to measure voltage and current, while a thermocouple positioned on the central cell measures the internal temperature.

Additionally, the external temperature was monitored using a thermal camera. The DUT's voltage, current, and power versus time graphs are presented in Figures 15–17, respectively. The temperature after the mechanical shock test is presented in Table 17.

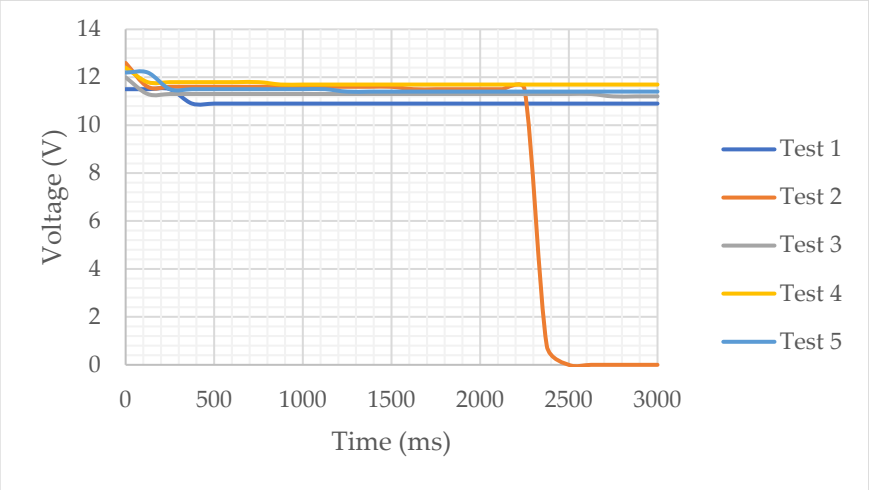


Figure 15. Voltage vs. Time.

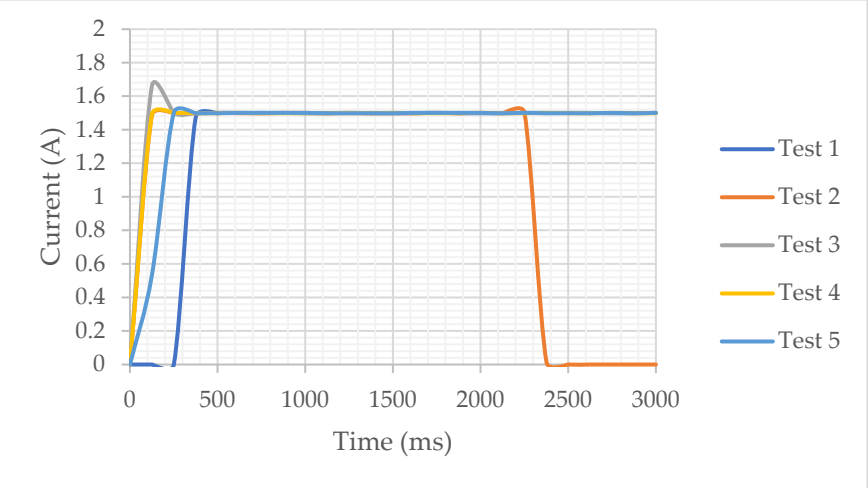


Figure 16. Current vs. Time.

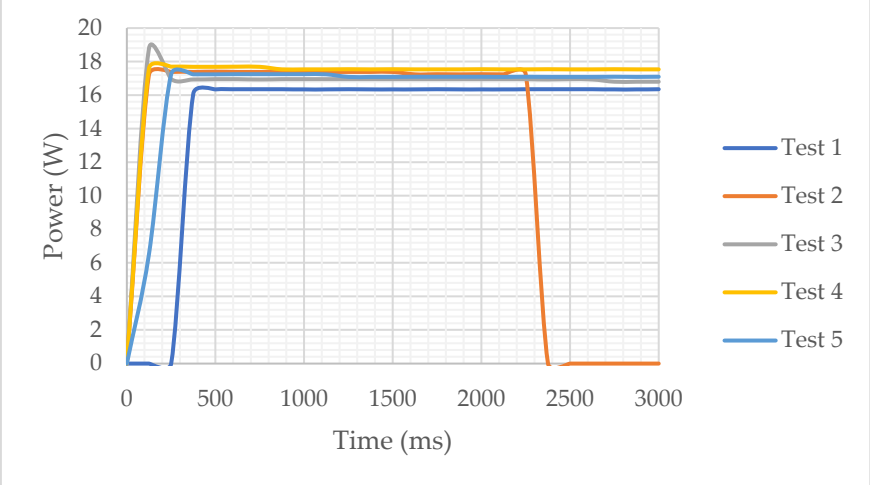


Figure 17. Power vs. Time.

Table 17. DUT's temperature after shock tests.

Test	1	2	3	4	5
Internal temperature (°C)	25.1	25	24.9	24.4	25.3
External temperature (°C)	28.5	28.3	28.3	28.2	28.5

3.4. Stresses and Deformations on Internal Cells

For the mechanical analysis, the longitudinal and hoop strains, as well as the principal stress, were measured on the cell case at the moment of impact. To carry out a quantifiable analysis on the effects of mechanical shock on the battery module, the use of strain gauges was proposed to measure the deformations caused by this physical phenomenon. Together with a specialized data acquisition system, the change in electrical resistance in these devices was measured, transforming it into resulting microdeformations in the analyzed material. This test method enables various experiments to be conducted with 18650 cells, regardless of their internal chemistry, in a non-invasive manner during battery operation.

For this purpose, a strain gauge rosette was installed in the central cell of each test module, as mentioned in Figure 9 of Section 2.4.3.

Due to this, three strain orientations are measured at an impact moment, and Figure 18, Figure 19, and Figure 20 present the strain measured on gauges A, B, and C, which are oriented at 0°, 45°, and 90°, respectively. Table 18 shows the strains measured in each test.

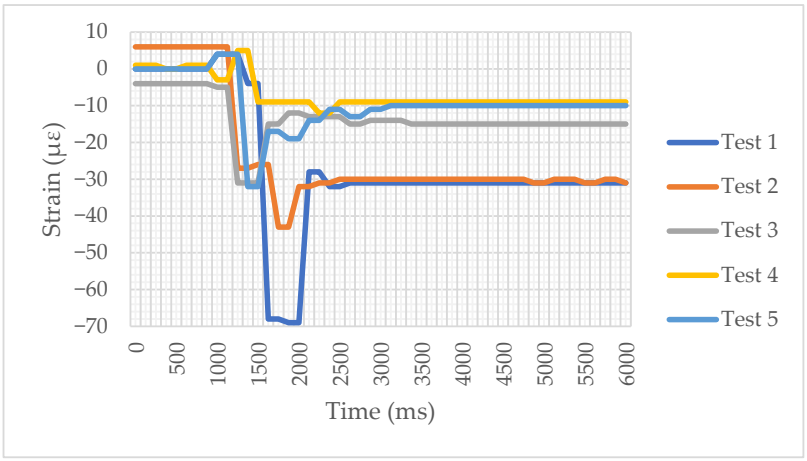


Figure 18. Strain-A vs. time.

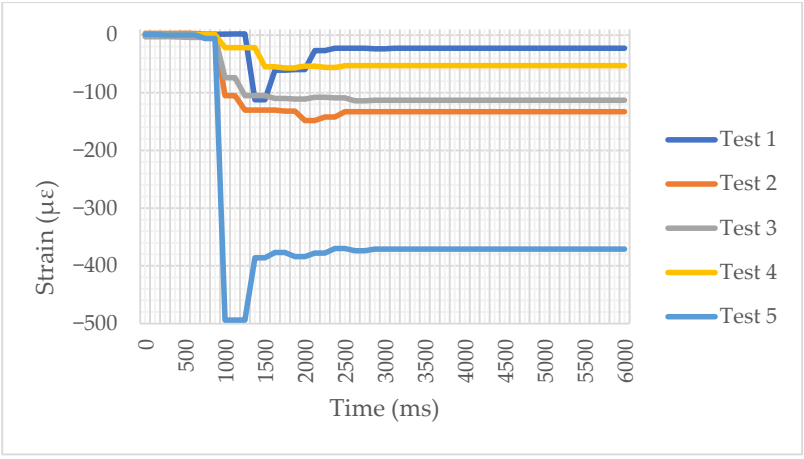


Figure 19. Strain-B vs. time.

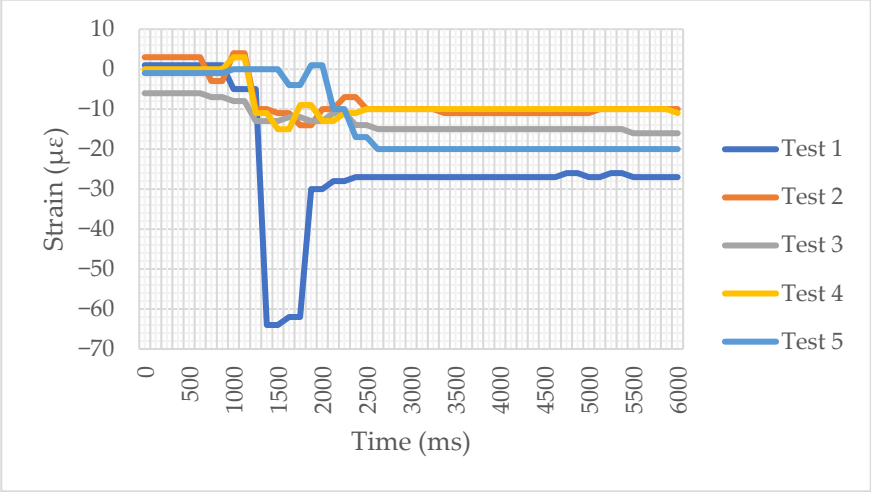


Figure 20. Strain-C vs. time.

Table 18. Strain measures achieved in tests.

Gauge's Strain	1	2	3	4	5
ε_a (με)	−4	−32	−15	−9	−14
ε_b (με)	−112	−148	−114	−57	−378
ε_c (με)	−64	−10	−15	−9	−10

Due to strain, rosettes are used to determine the state of plane stress at a point on a material's surface, where hoop and longitudinal strains are measured along the X and Y axes, respectively. The strain components were then calculated using the following equations:

$$\varepsilon_a = \varepsilon_x \times \cos^2\theta_a + \varepsilon_y \times \sin^2\theta_a + \gamma_{xy} \times \sin\theta_a \times \cos\theta_a \quad (6)$$

$$\varepsilon_b = \varepsilon_x \times \cos^2\theta_b + \varepsilon_y \times \sin^2\theta_b + \gamma_{xy} \times \sin\theta_b \times \cos\theta_b \quad (7)$$

$$\varepsilon_c = \varepsilon_x \times \cos^2\theta_c + \varepsilon_y \times \sin^2\theta_c + \gamma_{xy} \times \sin\theta_c \times \cos\theta_c \quad (8)$$

Table 19 presents the strain components calculated as a 3 × 3 equation system.

Table 19. Strain components in impact tests.

Strain Components	1	2	3	4	5
ε_x (με)	44	106	84	39	354
ε_y (με)	−112	−148	−114	−57	−378
γ_{xy} (με)	60	−22	0	0	−4

After this, the stress components can be calculated using Hooke's law for plane stress, as outlined in the following equations. Table 20 presents the calculated stress components.

$$\sigma_x = (E/1\text{-}\nu^2) \times (\varepsilon_x + \nu\varepsilon_y) \quad (9)$$

$$\sigma_y = (E/1\text{-}\nu^2) \times (\varepsilon_y + \nu\varepsilon_x) \quad (10)$$

$$\tau_{xy} = (E/2(1 + \nu)) \times (\gamma_{xy}) \quad (11)$$

Table 20. Stress components in impact tests.

Stress Components	1	2	3	4	5
σ_x (MPa)	2.389	19.98	14.65	6.47	66.86
σ_y (MPa)	−20.586	−25.86	−19.95	−9.92	−65.73
τ_{xy} (MPa)	4.419	−1.61	0	0	−0.29

After obtaining the stress components, the principal stress and the maximum shear stress were calculated. Table 21 presents the principal stress calculated.

$$\sigma_{1,2} = ((\sigma_x + \sigma_y)/2) \pm (((\sigma_x - \sigma_y)/2)^2 + {\tau_{xy}}^2)^{1/2} \quad (12)$$

$$\tan 2\theta_p = \gamma_{xy}/(\varepsilon_x - \varepsilon_y) \quad (13)$$

$$\tau_{max} = (((\sigma_x - \sigma_y)/2)^2 + {\tau_{xy}}^2)^{1/2} \quad (14)$$

Table 21. Principal stress in impact tests.

Principal Stress	1	2	3	4	5
σ_1 (MPa)	3.209	20.37	14.65	6.47	66.86
σ_2 (MPa)	−21.406	−26.25	−19.95	−9.92	−65.73
θ_p (°)	10.515	−4.86	0	0	0.06
τ_{max} (MPa)	12.308	23.31	17.3	8.195	66.3

To verify if the case material does not fail in the mechanical impact scenario, a Von Mises (VM) failure criterion was calculated with Equation (15). The criterion results are shown in Table 22 for each test.

$$\sigma_{VM} = ((\sigma_x)^2 - (\sigma_x \cdot \sigma_y) + (\sigma_y)^2 + (3{\tau_{xy}}^2))^{1/2} \quad (15)$$

Table 22. Von Mises criterion calculated.

Failure Criterion	1	2	3	4	5
σ_{VM} (MPa)	23.18	40.15	30.63	14.36	114.73

4. Discussion

Regarding the study object, as has been mentioned, the e-scooter is pre-owned, so the conditions of use of the battery module prior to purchase are unknown. Factors such as the drop, prolonged charging, or discharging of the battery module affect its lifetime.

The battery module consists of 80 cells, each with a capacity of 2 Ah, arranged in 16 cells per string and 5 strings per cell bank. With five cells in parallel, a coulomb capacity of 10 Ah is obtained, and the manufacturer reports a coulomb capacity of 12 Ah. So, the actual Coulomb capacity is 2 Ah lower than what the manufacturer reports on its datasheet.

The aging of the battery module was notorious. It was not possible to make a capacity test to verify its real capacity and SOH because it does not have a measurement instrument; its charge voltage measured was 64.1 V, which is lower than the charge voltage of a brand-new battery module according to the manufacturer's parameters (67.2 V). Although, in the voltage series, it was noted that in serial 2, in three cells, and in serials 6 to 10, all cells were below their discharge voltage. When analyzing the internal cells, it was found that

18 cells (22%) were below the discharge voltage reported by the manufacturer (2.75 V); the rest of the cells were within normal voltage values. This could occur due to a BMS malfunction, resulting in a balance issue in the cell's series, or if the battery charger used was not manufactured according to the manufacturer's specifications, which would affect the BMS functions. A future investigation testing the control and electronic systems in aged LEVs could help to understand how they contribute to the premature aging of internal cells.

In the cycling test, the 80 cells that made up the battery module were tested to measure their SOH. In this study, it was found that 46 cells (57%) had a SOH $\geq$ 80%, and 24 cells (30%) maintained a SOH $\geq$ 90%. On the other hand, seven cells (9%) stopped working within the first cycle. It should be noted that these cells were within the nominal voltage, in contrast to those with low voltage, which returned to the nominal voltage after a charging cycle. Regarding the remaining 27 cells (34%), their SOH was greater than 50%, so their useful life had ended, according to the datasheet. It should be noted that in the IR measurement, the cells presented an increase in resistance between 100 and 200% with respect to the original IR reported by the manufacturer ($\leq$30 mΩ); however, this was obtained with a smart charger that has a two-wire method of measurement, so the values could have a high degree of uncertainty.

Regarding lineal kinematics, Figure 13 shows the comparison of speed against time in the five tests carried out. At this stage, the acceleration lasted between 0 and 250 milliseconds (ms), as the tension in the elastic cords had been released. Consequently, a 1 G acceleration stage was entered, and the speed increased continuously to between 250 and 420 ms. Subsequently, the impact occurred, wherein the indenter abruptly lost speed until it reached 0 m/s. However, due to inertia, a rebound stage occurred, which took place between 420 ms and 600 ms, wherein negative velocities resulted from the movement of the indenter in the opposite direction to the fall, ultimately stabilizing. Figure 14 shows the comparison of acceleration against time in the five tests carried out. It should be noted that the semi-sinusoidal pulse part of the graph will be analyzed, as it is the primary focus of the study. This pulse occurred between 350 and 490 ms, where the start of each curve represents the acceleration before impact, and the peak corresponds to the maximum deceleration during impact. The average duration of these pulses is 53.6 ms. Maximum acceleration was measured by the change in direction, i.e., from maximum deceleration during impact to the maximum acceleration after impact. Additionally, the design data according to the regulations is a function of g-force, so the origin is positioned at the beginning of the curve, and the conversion from m/s^2 to g-force is carried out.

With respect to the electrical parameters, the DUTs were at 100% SOC. In Figure 15, a voltage drop peak, and a current surge peak are observed; therefore, power is shown in Figures 16 and 17, respectively. This is due to the power demand of 1.5 A DC during the tests. The moment of shock occurs between 2000 and 2500 ms, where test 2 presents a sudden drop in voltage, current, and power. This is due to the failure of the connection between the BMS and the XT-60 connector. With respect to the other modules, they did not present any change in their parameters at the time of the crash.

Regarding the thermal part, the internal and external temperatures of the modules were measured. The internal temperature was within a range of 25 $\pm$ 0.5 °C, whereas the external temperature record was in a range of 28 $\pm$ 0.5 °C. The temperature difference was due to the thermal camera recording the temperature of the BMS, which has a higher operating temperature than the cells.

In the mechanical analysis, Figures 18–20 show the records of microdeformations in gauges A, B, and C, respectively. In these graphs, the peak of the microdeformations occurs between 1000 and 2000 ms. In Table 18, the strain values are negative, which indicates the cells are being compressed during impact. The strain values varied across the tests, affecting

the DUTs differently due to the impact force. Test 5 showed the highest compressive strain in the cell's longitudinal face, this being -354 $\mu\varepsilon$. Utilizing the Von Mises failure criterion, it was confirmed that the casings of the tested cells exhibit no cracks from the applied impact, as the elastic limit of the casing material (A3 steel) is 250 MPa. Test 5 recorded the highest result at 114.73 MPa. It is worth highlighting that the DUTs inside the platform were fixed only on its Y-axis. When reviewing the slow-motion recordings, it was noted that the DUTs moved randomly, which could have altered the measurements of the gauges during the impact, as observed in test 5.

5. Conclusions

This work provides a critical new understanding of lithium-ion cell aging and mechanical shock response, quantifying the damage incurred at the cell level within an aging battery module of an electric scooter under mechanical shock conditions, such as those encountered in traffic accidents. More than half of the internal cells maintained an SOH of over 80%, and almost half of those cells had an SOH of $\geq$90%, indicating they remain within their useful life. However, there was a notable increase in their IR, leading to significant aging, even if the cells generally maintained capacity. This higher IR increases the risk to performance and might cause voltage drops and higher temperatures under high current loads. This parameter would have to be measured with high-precision equipment to verify and have a correct correlation.

Mechanical impact tests revealed a pattern of initial acceleration followed by a sharp deceleration upon impact, and a subsequent rebound phase. While most modules exhibited no instantaneous electrical failures during these tests, the observed random movement was attributed to insufficient mounting points and a mechanical measurement source of inaccuracy. Despite the failure criterion indicating that the casing material withstood mechanical impacts, the internal materials of the cells may fail, resulting in microcracks that could lead to internal short circuit. Therefore, a post-mortem study of the tested cells would be advantageous.

The single incident of a module connection failure highlights the importance of robust connection integrity in environments susceptible to shock. Although internal temperatures during testing remain constant, the temperature difference relative to external readings from the thermal camera, which is influenced by the running temperature of the BMS, underscores the importance of considering sensor location in future thermal investigations.

Author Contributions: Conceptualization, M.A.C.-P. and C.R.T.-S., methodology, J.C.P.-R.; software, J.A.F.-C.; validation, A.O.-O. and C.R.T.-S.; formal analysis M.A.C.-P. and C.R.T.-S., investigation, J.A.F.-C. and C.R.T.-S. resources J.A.F.-C. and C.R.T.-S.; data curation, J.C.P.-R. and C.R.T.-S.; writing—original draft preparation, M.A.C.-P. and C.R.T.-S.; writing—review and editing, M.A.C.-P. and C.R.T.-S.; visualization, A.O.-O.; supervision, J.C.P.-R. and C.R.T.-S.; project administration, A.O.-O. and C.R.T.-S.; funding acquisition, C.R.T.-S. All authors have read and agreed to the published version of the manuscript.

Funding: The authors wish to gratefully acknowledge the Secretaría de Ciencia, Humanidades, Tecnología e Innovación (SECIHTI), as well as support received by the National Polytechnic Institute through the projects SIP 20250106, SIP 20250288, SIP 20250033, as well as EDI grants. This research was performed in the CONAHCYT National Laboratory for Intelligent Electromobility (LANCEI: Laboratorio Nacional CONAHCYT en Electromovilidad Inteligente).

Institutional Review Board Statement: Not applicable.

Data Availability Statement: The original contributions presented in this study are included in the article. Further inquiries can be directed to the corresponding author.

Acknowledgments: The authors are thankful to the Instituto Politécnico Nacional and an EDI grant from SIP/IPN.

Conflicts of Interest: The authors declare no conflicts of interest.

Appendix A

Table A1. Electrical cell parameters obtained in the performance test.

Cell	Initial Voltage (V)	Charge Voltage (V)	IR (mΩ)	Capacity (mAh)	SOH (%)	Mass (g)
1s-1	3.95	0	0	0	0	45
1s-2	3.94	4.16	68	1221	61	44
1s-3	3.94	4.15	70	1377	69	45
1s-4	3.92	4.16	55	1386	69	44
1s-5	3.94	4.17	57	1551	78	45
2s-1	4.00	4.18	60	1739	87	45
2s-2	1.60	4.17	51	1667	83	45
2s-3	1.10	4.18	53	1604	80	44
2s-4	4.00	4.16	60	1648	82	44
2s-5	1.70	4.16	63	1612	81	44
3s-1	3.95	4.18	64	1709	85	44
3s-2	3.95	4.16	80	1623	81	45
3s-3	3.94	4.06	83	1483	74	44
3s-4	3.95	4.10	61	1642	82	44
3s-5	3.94	4.18	68	1552	78	44
4s-1	3.91	4.18	56	1630	82	45
4s-2	3.91	4.09	83	1548	77	44
4s-3	3.90	4.14	93	1634	82	44
4s-4	3.91	4.05	81	1519	76	44
4s-5	3.91	4.17	59	1619	81	45
5s-1	3.94	4.16	62	1377	69	44
5s-2	3.94	4.15	71	1267	63	45
5s-3	3.94	3.97	87	1411	71	44
5s-4	3.94	4.15	84	1437	72	44
5s-5	3.94	4.16	69	1357	68	45
6s-1	2.75	4.06	43	1604	80	44
6s-2	2.75	3.99	45	1618	81	44
6s-3	2.75	4.02	44	1529	76	44
6s-4	2.76	3.99	45	1695	85	45
6s-5	2.75	4.15	46	1560	78	44
7s-1	2.69	4.15	75	1855	93	45
7s-2	2.66	4.03	73	1879	94	44
7s-3	2.66	3.86	75	1843	92	44

Table A1. *Cont.*

Cell	Initial Voltage (V)	Charge Voltage (V)	IR (mΩ)	Capacity (mAh)	SOH (%)	Mass (g)
7s-4	2.65	3.96	74	1857	93	44
7s-5	2.65	4.13	77	1818	91	45
8s-1	2.72	4.16	93	1887	94	44
8s-2	2.72	4.15	90	1928	96	45
8s-3	2.72	3.85	93	1872	94	44
8s-4	2.72	3.95	88	1985	99	45
8s-5	2.72	3.32	94	1132	57	45
9s-1	1.60	4.16	60	1866	93	45
9s-2	1.68	4.08	64	1872	94	45
9s-3	1.60	4.18	63	1882	94	45
9s-4	1.69	4.15	68	1858	93	45
9s-5	1.60	4.17	57	1877	94	44
10s-1	2.75	4.06	87	1936	97	44
10s-2	2.75	3.97	84	1903	95	44
10s-3	2.75	3.98	84	1933	97	45
10s-4	2.75	4.17	88	1845	92	45
10s-5	2.75	4.17	63	1918	96	44
11s-1	3.91	4.06	69	1880	94	44
11s-2	3.91	3.95	78	1827	91	44
11s-3	3.91	3.96	74	1888	94	44
11s-4	3.91	4.13	77	1821	91	44
11s-5	3.91	4.17	67	1936	97	44
12s-1	3.93	0	0	0	0	44
12s-2	3.93	4.14	86	1079	54	44
12s-3	3.93	4.17	95	1175	59	45
12s-4	3.93	4.16	61	1421	71	44
12s-5	3.93	0	0	0	0	44
13s-1	3.93	4.16	79	1628	81	44
13s-2	3.93	4.16	90	1622	81	45
13s-3	3.93	4.16	58	1635	82	44
13s-4	3.91	4.16	99	1652	83	44
13s-5	3.93	4.15	61	1617	81	44
14s-1	3.90	4.17	57	1610	80	44
14s-2	3.90	4.17	55	1590	80	45
14s-3	3.90	4.16	81	1571	79	45
14s-4	3.90	4.16	65	1625	81	44
14s-5	3.90	4.16	78	1484	74	45
15s-1	3.88	0	0	0	0	45
15s-2	3.88	0	0	0	0	45

Table A1. *Cont.*

Cell	Initial Voltage (V)	Charge Voltage (V)	IR (mΩ)	Capacity (mAh)	SOH (%)	Mass (g)
15s-3	3.88	0	0	0	0	44
15s-4	3.88	0	0	0	0	44
15s-5	3.88	4.14	74	1221	61	45
16s-1	3.96	4.15	73	1368	68	45
16s-2	3.96	4.17	81	1332	67	44
16s-3	3.96	4.16	86	1209	60	45
16s-4	3.96	4.17	55	1485	74	44
16s-5	3.96	4.17	67	1413	71	44

References

1. Rode, P.; Burdett, R. Towards a Green Economy. United Nations Environment Program. 2011. Available online: https://wedocs.unep.org/bitstream/handle/20.500.11822/7979/GER_12_Cities.pdf?sequence=3&isAllowed=y (accessed on 20 January 2025).
2. United Nations. Goal 11: Make Cities Inclusive, Safe, Resilient, and Sustainable. 2022. Available online: https://www.un.org/sustainabledevelopment/cities/ (accessed on 20 January 2025).
3. Raczek, T. The Paris Declaration on Electromobility and Climate Change and Call to Action. 2015. Available online: https://unfccc.int/news/the-paris-declaration-on-electro-mobility-and-climate-change-and-call-to-action (accessed on 20 January 2025).
4. Chau, T.; Wang, K. An association between air pollution and daily most frequently visits of eighteen outpatient diseases in an industrial city. *Sci. Rep.* **2020**, *10*, 2321. [CrossRef] [PubMed]
5. Juginović, A.; Vuković, M.; Aranza, I.; Biloš, V. Health impacts of air pollution exposure from 1990 to 2019 in 43 European countries. *Sci. Rep.* **2021**, *11*, 22516. [CrossRef]
6. World Health Organization. The Top 10 Causes of Death. 2020. Available online: https://www.who.int/news-room/fact-sheets/detail/the-top-10-causes-of-death (accessed on 24 January 2025).
7. Mock, P. *World-Harmonized Light-Duty Vehicles Test Procedure (WLTP)*; Technical Report; International Council Clean Transportation: San Francisco, CA, USA, 2013.
8. ITF. Safer Micromobility. In *International Transport Forum Policy Papers, No. 129*; OECD Publishing: Paris, France, 2024.
9. Yannis, G.; Crist, P.; Petraki, V. *Safer Micromobility: Technical Background Report*; National Technical University of Athens: Zografou, Greece, 2024.
10. Oeschger, G.; Carroll, P.; Caulfield, B. Micromobility and public transport integration: The current state of knowledge. *Transp. Res. Part D Transp. Environ.* **2020**, *89*, 102628. [CrossRef]
11. Feng, C.; Jiao, J.; Wang, H. Estimating E-Scooter Traffic Flow Using Big Data to Support Planning for Micromobility. *J. Urban Technol.* **2020**, *29*, 139–157. [CrossRef]
12. MDCG DocsRoom—European Commission. Ongoing MDR IVDR Guidance Plan. 2020. Available online: https://ec.europa.eu/docsroom/documents/37824 (accessed on 28 January 2025).
13. Stark, J.; Meschik, M.; Singleton, P.A.; Schützhofer, B. Active school travel, attitudes and psychological well-being of children. *Transp. Res. Part F Traffic Psychol. Behav.* **2018**, *56*, 453–465. [CrossRef]
14. Møller, T.H.; Simlett, J. Micromobility: Moving Cities into a Sustainable Future. EY Report. 2020. Available online: https://www.ey.com/content/dam/ey-unified-site/ey-com/en-gl/insights/automotive/documents/ey-gl-micromobility-moving-cities-into-a-sustainable-future-01-2025.pdf (accessed on 7 July 2025).
15. Galatoulas, N.-F.; Genikomsakis, K.N.; Ioakimidis, C.S. Spatio-Temporal Trends of E-Bike Sharing System Deployment: A Review in Europe, North America and Asia. *Sustainability* **2020**, *12*, 4611. [CrossRef]
16. POLIS Macro Managing Micro Mobility. Available online: https://www.polisnetwork.eu/wp-content/uploads/2019/11/Polis-Paper-Macromanaging-MicroMobility.pdf (accessed on 31 January 2025).
17. McQueen, M.; Abou-Zeid, G.; MacArthur, J.; Clifton, K. Transportation Transformation: Is Micromobility Making a Macro Impact on Sustainability? *J. Plan. Lit.* **2020**, *36*, 46–61. [CrossRef]
18. Meigs, J.B. The Dark Side of "Micro-mobility"; Tragedies like this week's e-bike repair shop fire highlight the hidden dangers that personal vehicles powered by lithium-ion batteries pose to urban environments. *City J.* **2023**. Available online: https://link.gale.com/apps/doc/A779944225/AONE?u=anon~74a78fcf&sid=googleScholar&xid=bbeaebe4 (accessed on 3 February 2025).

19. Spielbauer, M.; Berg, P.; Ringat, M.; Bohlen, O.; Jossen, A. Experimental study of the impedance behavior of 18650 lithium-ion battery cells under deforming mechanical abuse. *J. Energy Storage* **2019**, *26*, 101039. [CrossRef]
20. Gehandler, J.; Karlsson, P.; Vylund, L. *Risks Associated with Alternative Fuels in Road Tunnels and Underground Garages*; SP Technical: Singapore, 2017.
21. Pan, Z.; Li, W.; Xia, Y. Experiments and 3D detailed modeling for a pouch battery cell under impact loading. *J. Energy Storage* **2020**, *27*, 101016. [CrossRef]
22. Ehsani, M. Modern Electric, hybrid Electric and fuel cell vehicles. In *Fundamentals, Theory and Design*; CRC Press: Boca Raton, FL, USA, 2010.
23. Automotive Cells Co. Battery Cell, Module or Pack. What's the Difference? 30 June 2022. Available online: https://www.acc-emotion.com/stories/battery-cell-module-or-pack-whats-difference-infographics (accessed on 12 February 2025).
24. Das, A.; Li, D.; Williams, D.; Greenwood, D. Joining Technologies for Automotive Battery Systems Manufacturing. *World Electr. Veh. J.* **2018**, *9*, 22. [CrossRef]
25. Wang, W.; Yang, S.; Lin, C.; Li, Y. Mechanical and electrical response of cylindrical Lithium-ion cells at various State of Charge. *Energy Procedia* **2018**, *145*, 128–132. [CrossRef]
26. Goodman, J.K.S.; Miller, J.T.; Kreuzer, S.; Forman, J.; Wi, S.; Choi, J.; Oh, B.; White, K. Lithium-ion cell response to mechanical abuse: Three-point bend. *J. Energy Storage* **2020**, *28*, 101244. [CrossRef]
27. Trattnig, G.; Leitgeb, W. Chapter 2: Battery modelling for crash safety simulation. In *Automotive Battery Technology*; Springer: Berlin, Germany, 2014; pp. 19–35.
28. Office of the New York City Comptroller Brad Lander. *Street Safety in the Era of Micromobility*; Government of New York City: New York, NY, USA, 2024. Available online: https://comptroller.nyc.gov/reports/street-safety-in-the-era-of-micromobility/ (accessed on 7 July 2025).
29. Qawasmeh, B. Micro-Mobility Safety Assessment: Analyzing Factors Influencing the Micro-Mobility Injuries in Michigan by Mining Crash Reports. *Future Transp.* **2024**, *4*, 1580–1601. [CrossRef]
30. Zhu, J.; Wierzbicki, T.; Li, W. A review of safety-focused mechanical modeling of commercial lithium-ion batteries. *J. Power Sources* **2018**, *378*, 153–168. [CrossRef]
31. Bisschop, R.; Willstrand, O.; Rosengren, M. Handling Lithium-Ion Batteries in Electric Vehicles: Preventing and Recovering from Hazardous Events. *Fire Technol.* **2020**, *56*, 2671–2694. [CrossRef]
32. Zhipeng, S.; Xiagjun, B.; Haishuo, M.; Tianyi, M. Comparative Study on Methods of Dynamic Crash Test of Power Batteries. *Adv. Nanosci. Nanotechnol.* **2021**, *5*, 5–9.
33. Zhao, W.; Luo, G.; Wang, C.-Y. Modeling Internal Shorting Process in Large-Format Li-Ion Cells. *J. Electrochem. Soc.* **2015**, *162*, A1352–A1364. [CrossRef]
34. Larsson, F. Lithium-Ion Battery Safety-Assessment by Abuse Testing, Fluoride Gas Emissions and Fire Propagation. Ph.D. Thesis, Chalmers University of Technology, Gothenburg, Sweden, 2017.
35. Fleischmann, C.; Weinschenk, C.; Madrzykowski, D.; Schraiber, A.; Gaudet, B. Quantifying the Fire Hazards of Lithium-Ion Battery Fires Caused by Thermal Runaway in E-Scooters. *FSRI*. 1 May 2025. Available online: https://fsri.org/research-update/journal-article-quantifies-fire-hazards-lithium-ion-battery-fires-caused-thermal (accessed on 18 June 2025).
36. Torelli, D.A.; Faenza, N.; Johns, P.; Lawton, S.; Frake, J. Evaluation of fire spread and suppression techniques in micro-mobility battery packs. *ECS Adv.* **2024**, *3*, 010501. [CrossRef]
37. Santhanagopalan, S.; Ramadass, P.; Zhang, J. Analysis of internal short-circuit in a lithium-ion cell. *J. Power Sources* **2009**, *194*, 550–557. [CrossRef]
38. Fuchs, G.; Willenberg, L.; Ringbeck, F.; Sauer, D.U. Post-mortem analysis of inhomogeneous induced pressure on commercial lithium-ion pouch cells and their effects. *Sustainability* **2019**, *11*, 6738. [CrossRef]
39. Li, L.; Chen, X.; Yuan, Q.; Wang, T.; Ji, H.; Papović, S.; Raleva, K.; Pan, F.; Yang, T.; Li, J. Effects of minor mechanical deformation on the lifetime and performance of commercial 21700 lithium-ion battery. *J. Electrochem. Soc.* **2022**, *169*, 060544. [CrossRef]
40. Sahraei, E.; Gilaki, M.; Lynch, W.; Kirtley, J.; Soudbakhsh, D. Cycling results of mechanically damaged li-ion batteries. In Proceedings of the 2019 IEEE Electric Ship Technologies Symposium (ESTS), Washington, DC, USA, 14–16 August 2019; pp. 226–230. [CrossRef]
41. *ANSI/CAN/UL/ULC 2271*; Batteries for Use in Light Electric Vehicle (LEV) Applications, UL 2271. Underwriters Laboratories: Northbrook, IL, USA, 7 September.
42. Charmant, J. "Features," Kinovea.org. [Online]. Available online: https://www.kinovea.org/features.html (accessed on 7 July 2025).

Disclaimer/Publisher's Note: The statements, opinions and data contained in all publications are solely those of the individual author(s) and contributor(s) and not of MDPI and/or the editor(s). MDPI and/or the editor(s) disclaim responsibility for any injury to people or property resulting from any ideas, methods, instructions or products referred to in the content.